



Originally published as:

Pick, L., Korte, M., Thomas, Y., Krivova, N., Wu, C. (2019): Evolution of Large-Scale Magnetic Fields From Near-Earth Space During the Last 11 Solar Cycles. - *Journal of Geophysical Research*, 124, 4, pp. 2527—2540.

DOI: <http://doi.org/10.1029/2018JA026185>

JGR Space Physics

RESEARCH ARTICLE

10.1029/2018JA026185

Key Points:

- The Hourly Magnetospheric Currents index (1900–2015) is a new measure for the signature of magnetospheric magnetic fields at ground level
- HMC resolves the absolute intensity of solar cycle variations more robustly than existing indices
- The open solar magnetic flux explains most of the low-frequency variability in HMC

Supporting Information:

- Supporting Information S1

Correspondence to:

L. Pick,
leonie.pick@gfz-potsdam.de

Citation:

Pick, L., Korte, M., Thomas, Y., Krivova, N., & Wu, C.-J. (2019). Evolution of large-scale magnetic fields from near-Earth space during the last 11 solar cycles. *Journal of Geophysical Research: Space Physics*, 124, 2527–2540. <https://doi.org/10.1029/2018JA026185>






Received 10 OCT 2018

Accepted 25 FEB 2019

Accepted article online 28 FEB 2019

Published online 5 APR 2019

Evolution of Large-Scale Magnetic Fields From Near-Earth Space During the Last 11 Solar Cycles

Leonie Pick¹ , Monika Korte¹ , Yannik Thomas¹ , Natalie Krivova² , and Chi-Ju Wu² 

¹GFZ German Research Centre for Geosciences, Potsdam, Germany, ²Max Planck Institute for Solar System Research, Göttingen, Germany

Abstract We use hourly mean magnetic field measurements from 34 midlatitude geomagnetic observatories between 1900 and 2015 to investigate the long-term evolution and driving mechanism of the large-scale external magnetic field at ground. The Hourly Magnetospheric Currents index (HMC) is derived as a refinement of the Annual Magnetospheric Currents index (HMC, Pick & Korte, 2017, <https://doi.org/10.1093/gji/ggx367>). HMC requires an extensive revision of the observatory hourly means. It depends on three third party geomagnetic field models used to eliminate the core, the crustal, and the ionospheric solar-quiet field contributions. We mitigate the dependency of HMC on the core field model by subtracting only nondipolar components of the model from the data. The separation of the residual (dipolar) signal into internal and external (HMC) parts is the main methodological challenge. Observatory crustal biases are updated with respect to AMC, and the solar-quiet field estimation is extended to the past based on a reconstruction of solar radio flux (F10.7). We find that HMC has more power at low frequencies (periods ≥ 1 year) than the Dcx index, especially at periods relevant to the solar cycle. Most of the slow variations in HMC can be explained by the open solar magnetic flux. There is a weakly decreasing linear trend in absolute HMC from 1900 to present, which depends sensitively on the data rejection criteria at early years. HMC is well suited for studying long-term variations of the geomagnetic field.

1. Introduction

Models of Earth's internally generated magnetic field have experienced considerable progress in the last two decades when high spatial resolution satellite data from dedicated missions (Ørsted, CHAMP, and SWARM) became available to complement the geomagnetic observatory record. This advance has now stalled due to the difficulties in properly accounting for external fields, that is, magnetic fields originating from outside of Earth (Finlay et al., 2017). On the timescale of the “historical era” (~1840 to now), this applies to large-scale fields that fluctuate at rates comparable to relatively rapid, subdecadal secular variation (SV) of the internal field (e.g., Gillet et al., 2010). These fields originate from electrical current systems in the inner and outer parts of the magnetosphere (recent reviews by Ganushkina et al., 2018; Milan et al., 2017).

Magnetospheric fields are often parameterized in spherical harmonic-based global field models using time variations from “geomagnetic activity” indices, derived from ground observatory data (Kauristie et al., 2017). For signals from the inner magnetosphere, the parameter traditionally used is the Dst index (Sugiura, 1964) or its corrected and extended version Dcx (Mursula & Karinen, 2005). However, it is well known that Dst (Dcx) is inappropriate for long-term modeling of the geomagnetic field, because its instable baseline (e.g., Olsen et al., 2005; Temerin & Li, 2015) causes an underestimation of the solar cycle variation in magnetospheric magnetic fields. In their magnetospheric field model, Lüher and Maus (2010) compensate for this effect using the 81-day running mean of the 10.7-cm solar radio flux (F10.7), lagged by ~20 months. In the context of this study it is important to understand the connection between solar magnetic and geomagnetic activity. The solar magnetic field emerges at the Sun's surface in form of active and smaller ephemeral magnetic regions (Harvey, 1994; Krivova & Solanki, 2004). Active regions dominate the variability on timescales up to a solar cycle (~11 years), whereas ephemeral regions are responsible for longer-term variations (Harvey, 1992; Solanki et al., 2000, 2002). Both sunspots (SN is the total sunspot number) and F10.7 originate from active regions and are good proxies of solar magnetic activity in general (e.g., Tapping, 2013). However, they do not represent well the longer-term changes in the solar magnetic field. Furthermore, SN and F10.7

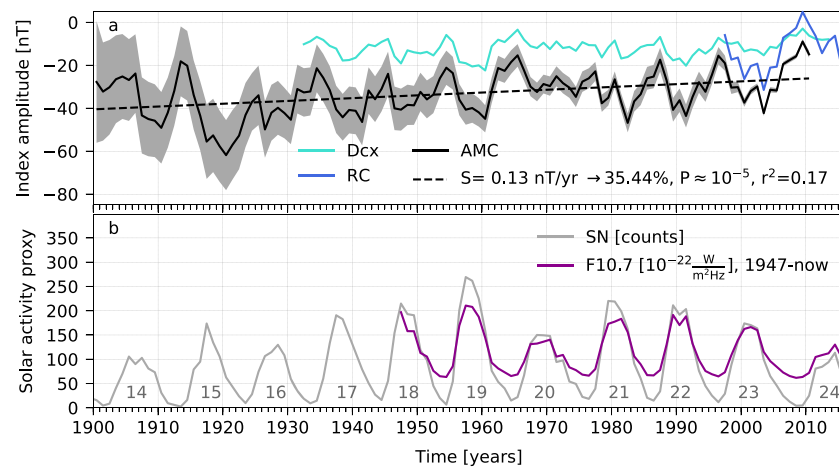


Figure 1. (a) AMC $\pm 3\sigma$ (black and gray; Pick & Korte, 2017) with linear fit (dashed) in comparison to annual means of Dcx (turquoise) and RC (blue). S , P , and r^2 are the slope, the p value for testing the null hypothesis, and the coefficient of determination, respectively. (b) Annual means of the total sunspot number (SN, gray) and absolute F10.7 flux (magenta) as proxies for solar magnetic activity. Solar cycles are numbered in gray. AMC = Annual Magnetospheric Currents index.

have no physical relation with the variability of magnetospheric magnetic fields, measured by geomagnetic activity indices like Dst. Geomagnetic activity ultimately results from the interaction of the near-Earth interplanetary magnetic field (IMF) with Earth's magnetic field. The source of the IMF is the so-called open solar flux (OSF), which is the part of the total solar magnetic field that leaves the Sun and enters the heliosphere in radial direction (e.g., Lockwood, 2013, details in section 2.2.2). This part includes contributions from both active and ephemeral regions. Consequently, OSF physically links solar and geomagnetic activities while being able to capture the long-term variability (>11 years) in the solar magnetic field.

The mentioned shortcomings of Dst motivated the creation of index alternatives for specific satellite-based model series, most importantly the Vector Magnetic Disturbances index (VMD, Thomson & Lesur, 2007) for the GFZ Reference Internal Magnetic Model series (GRIMM, most recent version by Lesur et al., 2015) and the scalar RC index (Olsen et al., 2014) for the CHAMP, Ørsted and SAC-C model series (CHAOS, most recent version by Finlay et al., 2016). Such efforts were expanded to the historical era by Pick and Korte (2017), who defined the scalar Annual Magnetospheric Currents index (AMC) covering the years 1900 to 2010 (Figure 1). While VMD and RC are developed to address the particular needs of their corresponding models, AMC is a stand-alone proxy for the absolute strength of magnetospheric currents at ground including uncertainty estimates.

AMC is particularly useful to reduce the contribution of magnetospheric disturbances in geomagnetic observatory data for studies of SV. However, a higher index cadence is needed to allow adequate use in combination with, for example, investigations of geomagnetic jerks (monthly resolution) or other standard geomagnetic field models and indices (hourly resolution). This is why we move from the AMC to the Hourly Magnetospheric Currents index (HMC). Wardinski and Holme (2011) and subsequently Brown et al. (2013) developed more elaborate methods to “denoise” observatory monthly means, but the advantages of the method are only fully brought to bear if a long-term high-quality reference station is available in the close vicinity of the observatory whose data are to be denoised. Going back in time, such data become increasingly scarce which is when HMC can contribute. Furthermore, HMC can help to address two open questions with respect to AMC that we discuss in this study.

Q1 A linear fit to AMC reveals a statistically significant decrease (absolute values) of 0.13 nT/year or 35% with respect to the level at 1900 (Figure 1a, dashed line). *Is the trend real, that is, did the magnetic effect of magnetospheric currents on Earth get weaker over time?*

Q2 A validation of [A/H]MC solar cycle dependent variability by a comparison to SN or F10.7 (Figure 1b) is unsatisfactory, as explained above. Given the established link between OSF and geomagnetic activity, *can the variability in [A/H]MC be traced back to that in OSF?*

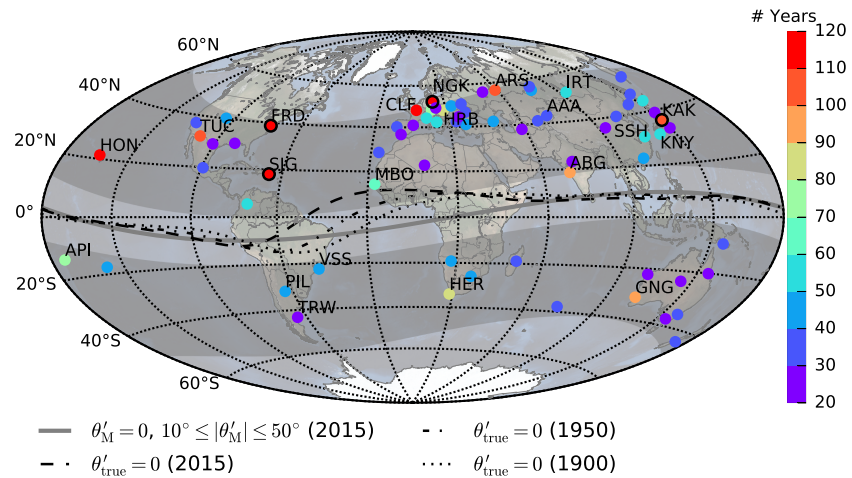


Figure 2. The 70 observatories and observatory clusters with the longest time series during 1900–2015 (color coded, maximum 116 years). For clusters only, the most recently active observatory is shown. HMC observatories (labeled) fall within 50° of mag latitude (θ'_M , gray shaded), excluding the geomagnetic equator (gray line for 2015). The position of the true magnetic equator ($\theta'_{true} = 0$) is calculated from IGRF-12 for 1900, 1950, and 2015 (black lines). AMC observatories are framed in black for reference. HMC = Hourly Magnetospheric Currents index; AMC = Annual Magnetospheric Currents index.

2. Data

2.1. Geomagnetic Data Used for HMC

The HMC index is based on hourly means of magnetic field measurements from 34 observatories obtained from the World Data Centre for Geomagnetism, Edinburgh with observatory locations made available by the International Association of Geomagnetism and Aeronomy (IAGA). We refer to specific observatories by their 3-letter IAGA codes (www.bgs.ac.uk/iaga/vobs).

For the best possible retrieval of the magnetospheric current signal, the observatories should cover different magnetic local times while avoiding high latitude disturbances (i.e., ionospheric auroral currents) and the ionospheric equatorial electrojet flowing along the magnetic equator on the dayside. Also, both hemispheres should be covered by data in order to mitigate hemispheric differences in the signal (e.g., Gannon, 2012). This places potential observatories in two midlatitudinal regions $10^\circ \leq |\theta'_M| \leq 50^\circ$ (Figure 2, gray shaded), with dipole latitude θ'_M in the geomagnetic coordinate system (mag , definition in Russell, 1971). Within these boundaries, we identified the longest time series from all observatories operating during the time span in question. These include composite time series from observatory clusters. On the one hand, such clusters consist of IAGA-designated predecessor-successor stations, for example, Cheltenham (CLH, Canada) and Fredericksburg (FRD, Canada). On the other hand, clusters are formed by observatories that are separated less than 300 km but are not officially replacing each other, for example, Wien Auhof (WIA, Germany) and Hurbanovo (HRB, Slovakia). The search radius of 150 km was selected as a typical upper bound between official predecessor-successor observatories (CLH and FRD are exceptionally far apart).

The observatories and clusters finally chosen to contribute to HMC are labeled in Figure 2. Caution is needed in case of the observatory M'Bour (MBO, Senegal) that is located within the realm of the South Atlantic Anomaly where the geomagnetic equator $\theta'_M = 0$ (gray line) deviates significantly from the “true” magnetic equator $\theta'_{true} = 0$ (black lines), calculated from IGRF-12 (Thébault et al., 2015). We verified that the characteristic features of HMC are not particularly sensitive to data from MBO (section 5.1).

An overview of the selected data is given in Figure 3. For this diagnostic plot, we subtracted the temporally varying core field contribution (from model COV-OBS.x1; Gillet et al., 2015) and static lithospheric biases (section 3.1) from the time series to facilitate the detection of spikes, jumps, and drifts by visual inspection. Spikes are single standout values, which we corrected if caused by obvious typos or else set to NaN (Not a Number). We eliminated sudden steps in the time series (“jumps,” e.g., Figure 3a, SVD) by joining the lower and upper edges of the step. Lastly, we identified times of smooth and gradual changes, spanning months to several years, that are unique to one particular observatory (“drifts,” e.g., Figure 3b, SSH). Such structures cannot be produced by magnetospheric sources and are consequently eliminated by subtracting either a

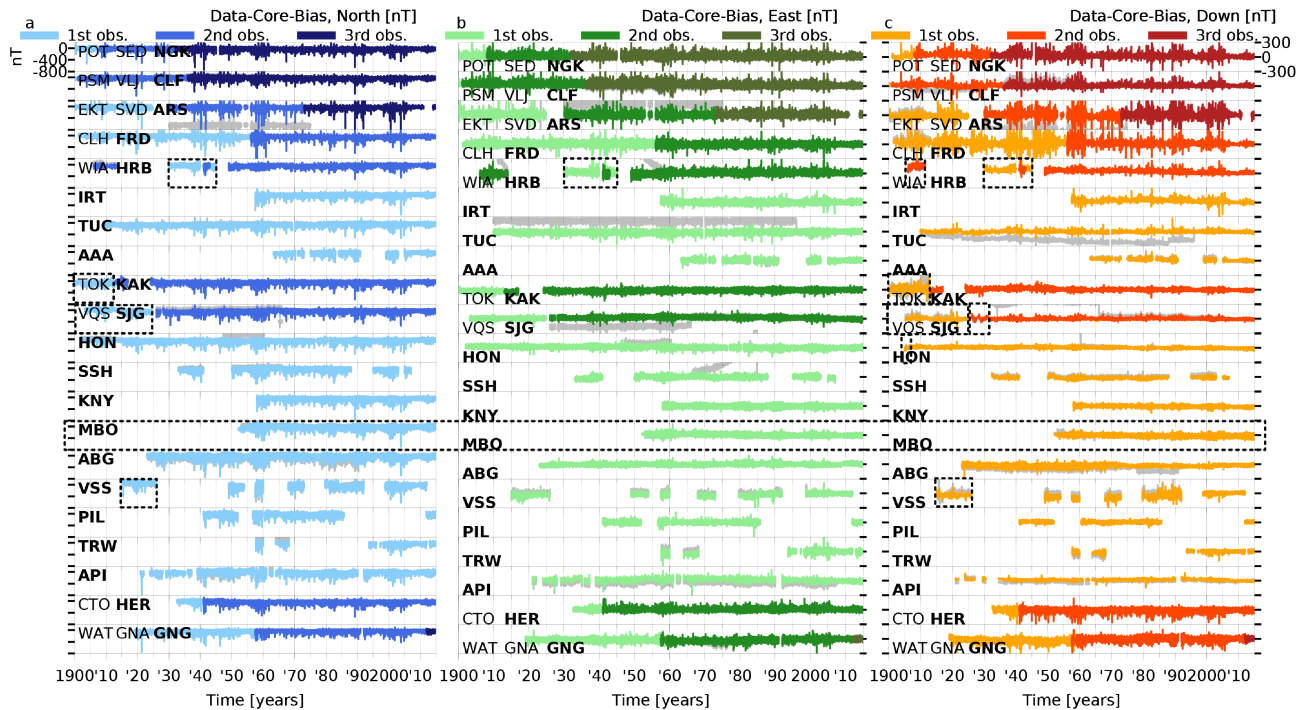


Figure 3. Residual magnetic field measurements (hourly) from observatories contributing to HMC. Local geodetic vector components point toward north (a, -800 to 200 nT), toward east (b, -300 to 300 nT), and vertically down (c, -300 to 300 nT). Time series from observatory clusters are color coded from light (earliest station) to dark (present station). Residua without modifications are shown in gray. Dashed boxes contain data segments of uncertain quality. HMC = Hourly Magnetospheric Currents index.

Polynomial or a Fourier fit to the data segment in question. Extensive modifications have been carried out particularly on the Z components from observatories VLJ, EKT, CLH, TOK, VQS, and VSS at early years. There are cases where the revised data still show characteristics not seen elsewhere in the same time series nor in any of the other observatories (dashed boxes in Figure 3). The influence of these segments on HMC as well as the drifts is discussed in section 5.1.

Finally, core and lithospheric contributions were again added to the altered residua to give a revised set of hourly means. Note that our data processing is tailored to isolate large-scale external field contributions. Signatures of either residual SV or artificial drifts cannot be differentiated and are both removed from the time series. Consequently, our revised set of hourly means is not appropriate for investigations of the internal geomagnetic field.

2.2. Proxies of Solar Magnetic Activity

2.2.1. The 10.7-cm Solar Radio Flux

The F10.7 flux is widely used in the field of geomagnetism to describe the influence of solar activity on the ionospheric magnetic field (Olsen, 1993). It is measured consistently on a day-to-day basis in Canada since February 1947, first by a radio telescope near Ottawa and then at the Dominion Astrophysical Observatory near Penticton. We have extended the record back to 1610 using the SATIRE-T model (Krivova et al., 2010; Wu et al., 2018). This model employs observations of sunspot numbers (since 1610) and areas (since 1876) to reconstruct the past evolution of the solar surface magnetic field as well as changes in the solar total and spectral irradiance. Past changes in F10.7 are then reconstructed through a regression analysis between the solar surface magnetic field and the measured F10.7 flux.

2.2.2. The Open Solar Magnetic Flux

The OSF is formed by that part of the solar magnetic field, which is blown out into the heliosphere where it threads a “coronal source surface,” usually taken to be a heliocentric sphere at $r_s = 2.5R_\odot$ (R_\odot is the mean solar radius). The “signed” OSF, that is, the flux of one radial field polarity, can be calculated as follows:

$$\text{OSF}(r_s) = 2\pi r_M^2 \langle |B_r(r_M)| \rangle_{>27^\circ} - E. \quad (1)$$

B_r is the radial component of the IMF pointing away from the Sun, equivalent to $-B_x$ in the Geocentric Solar Ecliptic frame. Averaging of $|B_r|$ over 27 days (one Bartels rotation) eliminates variations with coronal longitude. The excess flux E accounts for magnetic field contributions generated between the source surface (r_S) and the measurement point (r_M), which do not reflect the coronal source field. It is calculated from the longitudinal IMF component and the solar wind speed (v_{sw}) following Lockwood et al. (2009a, 2009b) to give the “kinematically corrected” OSF (equation (1)). All required quantities are taken from the OMNI-2 low-resolution (hourly averaged) data set, comprising measurements from near-Earth satellites at $r_M = 1$ AU (currently Wind, ACE) since November 1963. Due to data gaps in early years, a continuous record of the 27-day averaged kinematically corrected OSF starts in the beginning of 1974.

OSF is linked to HMC as follows (see review by Lockwood, 2013):

$$\text{OSF} \propto |B_r| \xrightarrow[\text{theory}]{1. \text{ Parker spiral}} B \cdot v_{sw} \xrightarrow[\text{coupling}]{2. \text{ sw-magnetosphere}} \text{HMC}. \quad (2)$$

B_r is connected to the magnitude of the IMF (B) and v_{sw} by Parker's (1958, 1963) spiral theory. The product $B \cdot v_{sw}^n$ quantifies the coupling between the solar wind and the magnetosphere (e.g., Finch & Lockwood, 2007), whereby an influx of solar wind particles alters magnetospheric current systems and triggers a response in HMC. Since the sensitivity to magnetospheric current systems varies among different indices, their correlation with $B \cdot v_{sw}^n$ peak for different n (Lockwood et al., 2013b). Relation 2 is valid for (a) an averaging time greater than 1 year (Stamper et al., 1999) and (b) a homogeneous response of the geomagnetic data to v_{sw} , that is, a constant optimum n (Lockwood et al., 2013a).

Lockwood et al. (2014) reconstruct OSF back to 1845 with an annual resolution in three steps: First, B and v_{sw} are reconstructed from the geomagnetic indices IDV(1d) (Lockwood et al., 2013a) and a corrected version of aa (aa_c), using connection 2 of relation 2 above. Second, $|B_r|$ is calculated using connection 1. Lastly, $|B_r|$ is regressed against the observed kinematically corrected OSF (equation (1)) to give the kinematically corrected, reconstructed OSF (see supporting information Text S3).

3. Methodology

The modeling strategy follows the derivation scheme of AMC, which assumes the field produced by magnetospheric currents to be large-scale, that is, being represented by spherical harmonic (SH) degree $N = 1$, and axisymmetric with respect to the dipole axis. We use all local times, including daytime observatories, and the full vector, including the vertical downward component (Z). This is because we prioritize the use of all available data carrying the signal in question over the avoidance of ionospheric fields (during daytime) and the induced signal (Z), which are globally heterogeneous. Furthermore, a proper treatment of induced signal requires an appropriate conductivity model, possibly a 3-D model to account for the “ocean effect” (Grayver et al., 2017), and we would like to leave this choice to the user of HMC.

3.1. Processing

First, we calculate residua $\vec{B}_i(t)$ for all observatory time series, $i = 1, \dots, N_o$ (maximum N_o is 21), by subtracting estimates for the core field, $\vec{B}_c(t)$, the midlatitude ionospheric field, $\vec{B}_i(t)$, and the static, high-degree crustal field, \vec{B}_b , from the revised observatory data $\vec{B}_o(t)$:

$$\vec{B}_i(t) = \vec{B}_o(t) - (\vec{B}_{cND,i}(t) + \vec{B}_i(t) + \vec{B}_b), \quad (3)$$

$$\vec{B}_b = (\vec{B}_o(t) - (\vec{B}_c(t) + \vec{B}_i(t) + \vec{B}_e(t)))_{[1999, \dots, 2015], \text{ quiet \& dark}} \quad (4)$$

For the core field, the choice of COV-OBS.x1 is practically without alternative as there is no other published core field model covering the historical era up to the present. HMC is particularly sensitive to the dipole component ($N = 1$) of this core field model. We therefore do not subtract the complete model but only the nondipole model part corresponding to SH degrees $N = 2, \dots, 14$, $\vec{B}_{cND,i}(t)$. This way we do not need to assume that COV-OBS's internal dipole component is correct, and we can perform the separation of signal into internal and external contributions ourselves.

As we include daytime data, we need to remove as far as possible the midlatitude ionospheric field $\vec{B}_i(t)$ peaking around local noon when photoionization by the Sun maximizes. This field causes the so-called

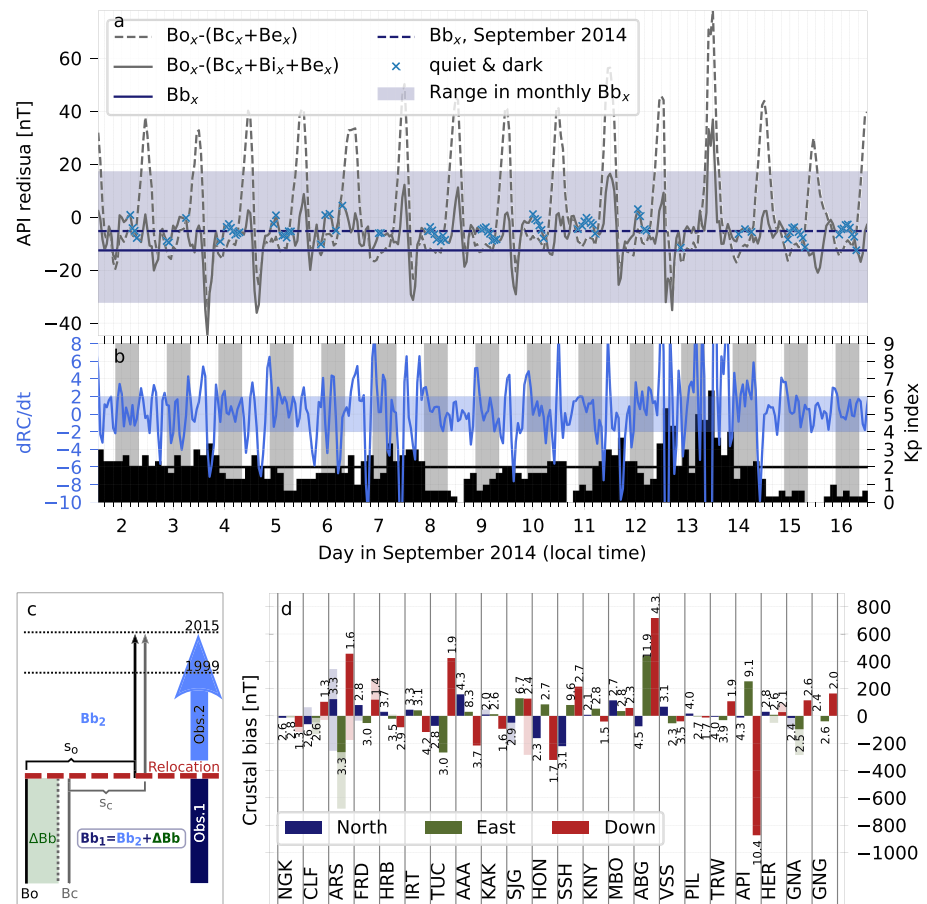


Figure 4. (a) Measurement residua and crustal bias at Apia observatory (API). Residua before (gray dashed) and after (gray solid) CM4 was removed with data points for crustal bias calculation (blue crosses). Final bias (blue solid) and short-term bias (blue dashed) fall within a 49.2 nT wide range (blue shaded) spanned by all short-term biases. (b) Quiet ($|dRC/dt| \leq 2.0$, blue; $Kp \leq 2^0$, black) and dark (solar elevation angle $\leq -10^\circ$, gray) selection criteria for crustal bias data. (c) Sketch illustrating the calculation of the crustal bias (Bb_1) for an observatory (Obs. 1), that was relocated prior to 1999 (thereafter Obs. 2) from differences in measurements (s_0) and core field estimates (s_c) at the two sites (see text and equation (5)). (d) Crustal biases (bars) with median absolute deviations (small labels), see Table S1. Biases for predecessors are shown in faded colors.

solar-quiet variations (e.g., Yamazaki & Maute, 2017), and we consider it in a climatological sense by the CM4 model (Sabaka et al., 2004). CM4 can be evaluated outside of the validity interval of the corresponding core field description (1960–2002) with appropriate values for the monthly mean F10.7 flux (3-month moving averages). To this end, we supplement the record of measured F10.7 flux (starting in 1947) with reconstructed F10.7 flux starting in 1900 (section 2.2.1). An example of solar-quiet variations in the northward component (X) at Apia observatory (API, Western Samoa) for 15 days in September 2014 is shown in Figure 4a before (gray dashed) and after (gray solid) CM4 has been subtracted. The amplitude of the variation clearly reduces, although CM4 cannot handle the day-to-day variability.

For the crustal biases, \bar{Bb}_i , we use the CHAOS model (version 6, Finlay et al., 2016) to estimate the recent internal ($\bar{Bc}_i(t)$) and external magnetospheric ($\bar{Be}_i(t)$) field contributions in equation (4). Considering $\bar{Be}_i(t)$ ensures a correct baseline level of HMC (see Pick & Korte, 2017, section 3.1). We apply the same criteria for selecting geomagnetically quiet ($Kp \leq 2^0$, $|dRC/dt| \leq 2.0$) and dark (Sun at least 10° below horizon) periods as are applied in CHAOS-6 for vector field data at midlatitudes. The bias vector is calculated for each observatory from the median of the selected data points within the period 1999–2015. This procedure is illustrated for the X component by the example of API in Figures 4a and 4b. If the northward bias had instead been calculated from the first 15 days of each month within the period 1999–2015 (“short-term” bias), there would be a ~ 50 nT wide spread in the results for API representing the dependency on season and

solar cycle phase. API is the observatory most sensitive to these modulations (across all components) which is why we show it as “worst case” in terms of bias estimation. However, when considering the whole time span, 1999–2015, the median absolute deviation of biases for all observatories is about an order of magnitude smaller, that is, ≤ 4.5 nT for X, ≤ 11.9 nT for Y, and ≤ 10.4 nT for Z (Figure 4d and Table S1). We conclude that our estimation of crustal biases is robust and justify the use of the CHAOS-6 core field estimate by a slightly smaller cumulative median absolute deviation as compared to the COV-OBS.x1 estimate.

A problem arises for those observatories in clusters that are not active during 1999–2015. In such cases, we follow a procedure illustrated in Figure 4c. For official predecessor-successor observatories, the step in measurements (\vec{s}_o) between observatory 1 ($\vec{B}b_1$ not known) and observatory 2 ($\vec{B}b_2$ known) at the time of the relocation is documented in the observatory annual means file provided by the British Geological Survey. In the case of WIA and HRB, we calculated \vec{s}_o directly from the annual mean data for 1941 and check the influence of this alternative method in section 5.1. Since the external fields should not vary significantly between the two locations, the step can be assumed to result from a difference in the core and crustal field (crustal bias) contributions. We estimate the difference in the core field contribution with COV-OBS.x1 (\vec{s}_c) and find the crustal bias of observatory 1 as

$$\vec{B}b_1 = \vec{B}b_2 + (\vec{s}_o - \vec{s}_c) = \vec{B}b_2 + \Delta Bb. \quad (5)$$

In a last processing step, the observatory residua \vec{B}_i are transformed from the measurement coordinate system (spheroidal *ned*: latitude- θ_d , longitude- ϕ , height- h & North- X , East- Y , Down- Z) into a geocentric system (spherical *seu*: colatitude- θ_c , longitude- ϕ , radius- r & South- B_θ , East- B_ϕ , Up- B_r). All coordinate system transformations involved follow the nomenclature detailed in both equation (3) and Table A1 of Pick and Korte (2017).

3.2. Modeling

Having calculated the residua time series for each observatory, we combine them in one data vector \vec{B} per universal time hour (in the *seu* system). We assume the residua to arise from a Laplacian vector field that is expressed as the gradient of a scalar potential V :

$$\vec{B} = -\nabla V. \quad (6)$$

The potential is expanded in spherical harmonics up to degree (N) and order (m) one and composed of an internal ($\sim (a/r)^{n+1}$) and an external ($\sim (r/a)^n$) part according to the radial distance of the observation from the reference level at the Earth's surface ($a = 6,371.2$ km):

$$V = V_{\text{int}} + V_{\text{ext}} = \Re \left\{ a \sum_{n=1}^N \sum_{m=0}^n \left[i_n^m \left(\frac{a}{r} \right)^{n+1} + \epsilon_n^m \left(\frac{r}{a} \right)^n \right] P_n^m(\cos \theta_c) e^{im\phi} \right\}. \quad (7)$$

P_n^m are the Schmidt quasi-normalized associated Legendre polynomials and i_n^m, ϵ_n^m are the internal and external Gauss coefficients:

$$i_n^m = g_n^m + ih_n^m, \quad \epsilon_n^m = q_n^m - is_n^m. \quad (8)$$

The forward problem is

$$\mathbf{G}\vec{x} + \vec{\epsilon} = \vec{B}, \quad (9)$$

where matrix \mathbf{G} relates the observations \vec{B} , including uncertainties $\vec{\epsilon}$, to the model coefficients \vec{x} . After the processing described by equation (3), we expect that the residua result from an $N = 1$ internal field overlain by an external field contribution best described in geomagnetic coordinates (*mag*: θ_M, ϕ_M, r_M & $B_{\theta,M}, B_{\phi,M}, B_{r,M}$). Thus, the coefficients vector consists of the three internal dipole coefficients (*seu* system) and the external axial dipole coefficient (*mag* system):

$$\vec{x} = (g_1^0, g_1^1, h_1^1, q_{1M}^0)^T. \quad (10)$$

$$\text{HMC} := -q_{1M}^0. \quad (11)$$

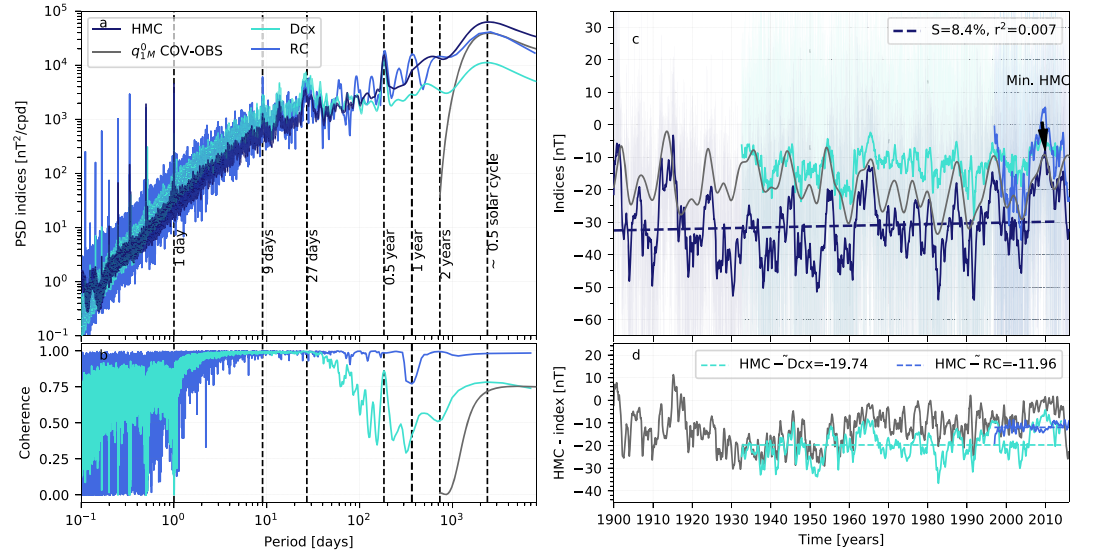


Figure 5. (a) Power spectral densities (PSD) of HMC, Dcx, RC, and q_{1M}^0 COV-OBS (≥ 2 years). (b) Magnitude squared coherence of HMC and either Dcx, RC, or q_{1M}^0 COV-OBS (≥ 2 years). (c) Low-pass filtered (cutoff 1 year) HMC with linear fit (dashed), Dcx, RC, and q_{1M}^0 COV-OBS atop the corresponding hourly values (faded). HMC minimum (absolute value) of -7.78 nT at 2009 (arrow). (d) Differences between HMC and either Dcx, RC, or q_{1M}^0 COV-OBS together with the median of the differences (dashed). HMC = Hourly Magnetospheric Currents index.

The latter is what we define as HMC index, where the minus sign indicates that it is a southward-directed field.

The corresponding matrix \mathbf{G} has dimensions $(3N_o \times 4, N_o: \text{number of observatories})$ with the following entries:

$$\mathbf{G} = \begin{pmatrix} -\left(\frac{a}{r}\right)^3 \frac{dP_1^0}{d\theta} & -\left(\frac{a}{r}\right)^3 \cos(\phi) \frac{dP_1^1}{d\theta} & -\left(\frac{a}{r}\right)^3 \sin(\phi) \frac{dP_1^1}{d\theta} & -\frac{dP_1^0}{d\theta} \\ 0 & \left(\frac{a}{r}\right)^3 \sin(\phi) \frac{P_1^1}{\sin \theta} & -\left(\frac{a}{r}\right)^3 \cos(\phi) \frac{P_1^1}{\sin \theta} & 0 \\ \left(\frac{a}{r}\right)^3 2P_1^0 & \left(\frac{a}{r}\right)^3 2\cos(\phi)P_1^0 & \left(\frac{a}{r}\right)^3 2\sin(\phi)P_1^0 & -P_1^0 \\ \vdots & \vdots & \vdots & \vdots \\ \underbrace{\frac{d}{dg_1^0}, seu}_{\frac{d}{dg_1^0}, seu} & \underbrace{\frac{d}{dg_1^1}, seu}_{\frac{d}{dg_1^1}, seu} & \underbrace{\frac{d}{dh_1^1}, seu}_{\frac{d}{dh_1^1}, seu} & \underbrace{\frac{d}{dq_{1M}^0}, mag \rightarrow seu}_{\frac{d}{dq_{1M}^0}, mag \rightarrow seu} \end{pmatrix}. \quad (12)$$

In order to coestimate the internal and external Gauss coefficients, the column of \mathbf{G} which relates to the external coefficient (column 4) has to be estimated using *mag* coordinates for the observatory positions. Subsequently, the vectors corresponding to each observatory i (rows 1–3, 4–6, ...) have to be transferred back to the *seu* system.

We invert the problem in equation (9) using a simple iterative least squares fit (details in Text S1):

$$\hat{\mathbf{x}}_{k+1} = \left(\mathbf{G}(\hat{\mathbf{x}}_k)^T \mathbf{G}(\hat{\mathbf{x}}_k) \right)^{-1} \mathbf{G}^T(\hat{\mathbf{x}}_k) \bar{\mathbf{B}}. \quad (13)$$

We do not treat the uncertainties of the observatory residua $\vec{\epsilon}$ here. For AMC, we have assumed that data uncertainties are normally distributed and simply weighted matrix \mathbf{G} with the residua covariance matrix at each inversion time step. For HMC, this procedure comes at a high computational cost given that the inversion is performed at each UT hour (1,016,832 time steps). This effort is unnecessary provided the long-term uncertainty characteristics remain unchanged when stepping down to hourly means (i.e., AMC uncertainties apply) or the method to calculate index uncertainties is not profoundly revised.

4. Results

The questions Q1 and Q2 target long-term characteristics of HMC, that is, low-frequency variations in HMC. We analyze HMC's spectral content in terms of the power spectral density (PSD) and use the magnitude

squared coherence to compare HMC to Dcx, RC, and q_{1M}^0 from COV-OBS.x1 (section 4.1). Low-pass filtered versions of HMC and the other quantities are then investigated in the time domain (section 4.2). Text S2 provides information on the internal dipole coefficients.

4.1. HMC in the Frequency Domain

The PSDs of the different magnetospheric field measures (Figure 5a) are calculated from the maximum available time series, so that frequency bins for HMC (since 1900) are most narrow, followed by Dcx (since 1933) and RC (since 1997). The shape of the PSDs for the different proxies is similar with known peaks, prominently at 1, 9, and ~ 27 days as well as half a sidereal year (365.256 days). All PSDs show a broad maximum centered approximately at half a solar cycle. HMC shows greater power at periods ≥ 1 year than the other quantities. Thus, we fix the cutoff frequency for the low-pass filter at $1/(365.256 \text{ days}) \sim 3.2 \cdot 10^{-8} \text{ Hz}$.

Dcx shows high power between ~ 9 days and 1 month, but the power decreases notably at longer periods relative to the other measures. This confirms that Dcx lacks long-term variability as a consequence of its erroneous baseline (section 1). RC is the most variable, showing multiple peaks, that are either absent or very small for the other quantities, especially at periods below 1 day and greater than ~ 50 days. This could be connected to the use of only night side data. q_{1M}^0 COV-OBS is part of a model parameterized in time by cubic B-splines with a 2-year knot spacing. Therefore, its energy content is meaningful for periods ≥ 2 years and becomes comparable to that of the other indices not until periods ≥ 3 years.

The coherence analysis (Figure 5b) reveals a very high degree of similarity (close to one) in the frequency contents of HMC and RC, except for some notches caused by RC variability not present in HMC (most prominently at a 1-year period). The coherence for HMC and Dcx exhibits a plateau-like shape with large values for periods between few days and a month and a rapid decrease to below 0.5 for larger periods. Due to the different temporal resolutions, the coherence of HMC and q_{1M}^0 COV-OBS does not get larger than ~ 0.75 at periods relevant to the solar cycle.

4.2. HMC in the Time Domain

We now compare the low-pass filtered HMC to the other indices and q_{1M}^0 COV-OBS in the time domain. Regarding the long-term trend (Q1) we find that much of the linear decrease in absolute AMC (35%) is gone leaving only a small, albeit significant, decrease in absolute HMC of 8.41% (Figure 5c). We attribute the weakening of the trend to the data modifications performed and discuss the sensitivity of HMC to these alterations as well as the robustness of the long-term trend in section 5.1.

HMC is generally more negative than RC and Dcx, with a recent absolute minimum of -7.78 nT reached on 3 December 2009 at the beginning of solar cycle 24 (Figure 5c). The smallest absolute AMC is only $\sim 1 \text{ nT}$ larger that year, although the underlying observatory annual means include geomagnetically disturbed times. This means that occurrences of geomagnetic storms do not effectively alter the magnetospheric signal's background level. The differences between HMC and the other quantities are shown in Figure 5d. The median difference between RC and HMC is -11.96 nT , which agrees with the offset found between AMC and RC and thereby implies that HMC's absolute level is reasonable (Pick & Korte, 2017). The offset between Dcx and HMC is considerably larger (-19.74 nT). Solar cycle dependent offsets calculated for Dst in the order of -15 nT (Lühr & Maus, 2010; Temerin & Li, 2015) do not apply, because Dcx corrects for the so-called "nonstorm component" (Karinen & Mursula, 2006), shifting the index to more positive values on average.

Differences between q_{1M}^0 COV-OBS and HMC (Figure 5d, gray) are structured in three parts with a moderate difference level until ~ 1935 , large differences up to 30 nT between 1935 and 1965 and comparably small differences afterward. These "steps" in the offsets could be due to the different data bases for COV-OBS.x1 and HMC. COV-OBS.x1 uses annual mean observatory measurements which do not reveal data problems as clearly as hourly means do. The deviations prior to 1935 could therefore be caused by our data modifications that are not accessible to COV-OBS.x1. Satellite data are used in COV-OBS.x1 starting with the POGO series, which could explain the step in the 1960s.

5. Discussion

In this section we discuss the influence of the data modifications on HMC's low-frequency variability (Q1, section 5.1) and to what extent this variability can be traced back to OSF (Q2, section 5.2).

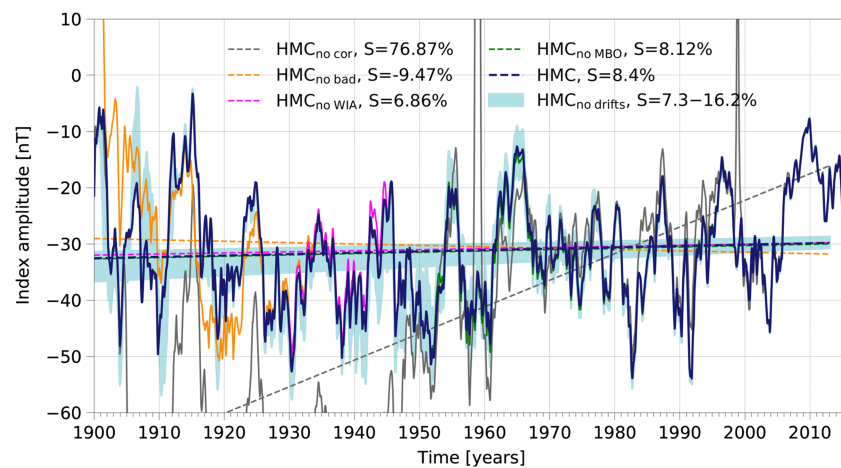


Figure 6. Comparison of HMC (dark blue) to index versions based on different data sets with linear fits. (no cor) No data manipulations as shown in Figure 3, gray. (no bad) Data segments circled in Figure 3 are discarded (apart from MBO and WIA). (no WIA and no MBO) All data from WIA or MBO observatories are discarded. (no drifts) Spread in results for data with drift removal (HMC) and without drift removal in either X, Y, and Z or all components. HMC = Hourly Magnetospheric Currents index.

5.1. Sensitivity of HMC to Data Modifications and Robustness of Long-Term Trend

First, we define $HMC_{no\ cor}$, which includes no data manipulations apart from the removal of large spikes in the original .wdc files. $HMC_{no\ cor}$ and the final HMC (including all modifications) are compared in Figure 6. These versions differ significantly during 1905–1947, moderately during 1947–2003, and insignificantly afterward. Special attention has to be paid to the influence of our drift removal (section 2.1) on the inferred long-term trend in HMC. $HMC_{no\ drift}$ gives the spread in results obtained from data with drift removal (HMC) and without drift removal in either X, Y, or Z or all components (five versions). In accordance with the final HMC, the inferred trends consistently indicate a decrease in absolute value, varying between 7.3% and 16.2% since 1900. We can thus conclude that the detected weakly positive trend in HMC is most likely genuine, that is, not an artifact of our data modifications.

While it is expected that the data modifications as a whole improve the result, the effect of some problematic data segments or specific observatories (Figure 3, dashed boxes) is not obvious. Figure 6 shows versions of HMC that do not include unreliable looking data ($HMC_{no\ bad}$), data from WIA observatory ($HMC_{no\ WIA}$), and data from MBO observatory ($HMC_{no\ MBO}$). Based on these test runs, we can rule out that the alternative method to determine the crustal bias for WIA or the possible presence of disturbances from the equatorial electrojet in the data of MBO significantly alter the result. However, discarding the unreliable data segments significantly changes the index prior to ~1935 (HMC vs. $HMC_{no\ bad}$) so that the overall trend flips from positive (blue dashed) to negative (orange dashed). The fact that $HMC_{no\ bad}$ reaches unrealistically large positive values made us keep all data and associated data modifications in the final version of HMC.

5.2. OSF as Driver for HMC Variability

A detailed comparison between HMC and OSF (Q2) is shown in Figure 7. In contrast to HMC, the reconstructed OSF shows a linear increase (absolute values) of 31.46% since 1900 (Figures 7a and 7b). The major difference between these trends originates from the period 1935–1965, during which HMC and OSF exhibit oppositely directed trends (Table 1).

Figures 7c and 7d show the coefficient of determination (r^2) between OSF and either HMC, q_{1M}^0 , COV-OBS, Dcx, or RC for annual means (Figure 7c, OSF reconstructed) and 27-day means (Figure 7d, OSF measured). r^2 is calculated on different timescales, starting with values since 1900 (left) and ending with values since 1997 (right). An example of the underlying linear regressions is given in Figure 7e, showing HMC versus OSF since 1997 (measured) and since 1900 (reconstructed) with corresponding linear fits. In both cases, ~60% of the variability in HMC can be explained by OSF. Three pieces of information can be extracted from Figures 7c–7e in total. First, OSF is related to annual means of geomagnetic indices more closely (greater r^2) than to 27-day means (e.g., 0.96 for annual means and 0.62 for 27-day means since 1997). This is expected,

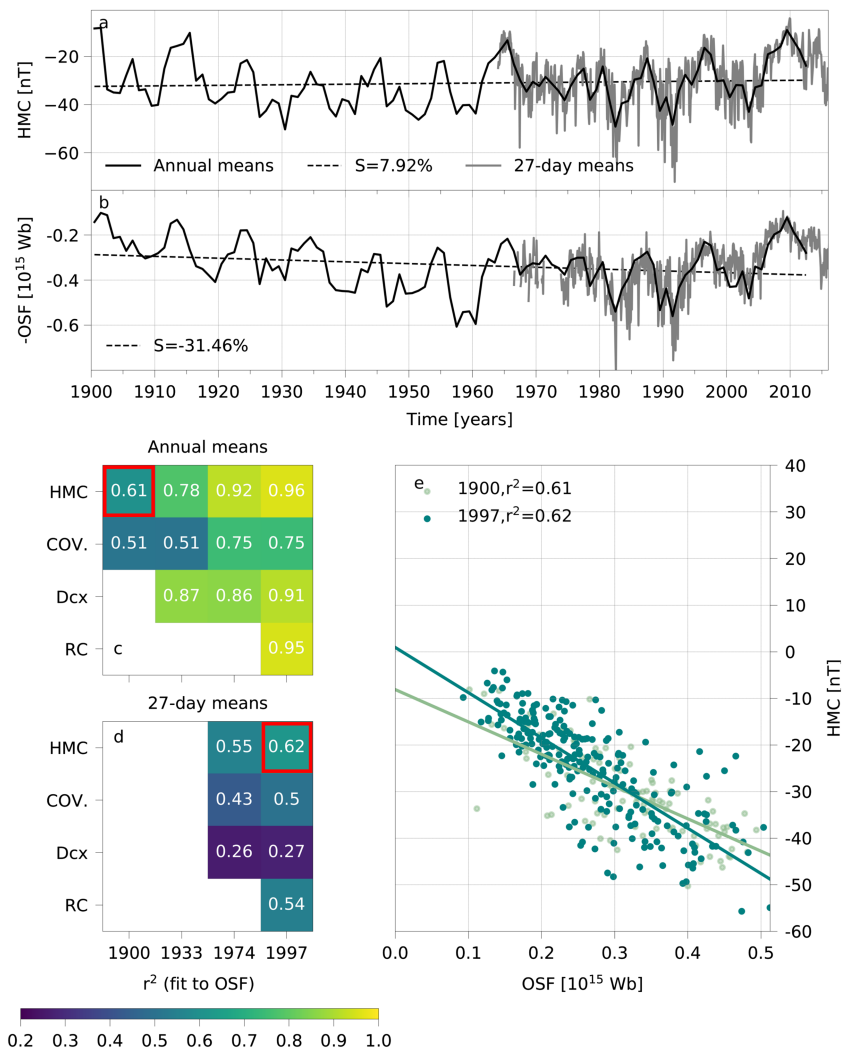


Figure 7. (a and b) Annual and 27-day means of HMC and the kinematically corrected OSF with linear fits. Annual values for OSF are taken from its reconstruction (section 2.2.2). (c and d) Coefficients of determination (r^2) for OSF (c: reconstructed, d: measured) and either HMC, q^0_{1M} COV-OBS.x1 (COV), Dcx, or RC for four different time intervals—since 1900 (full), since 1933 (start Dcx), since 1974 (start continuously measured OSF), and since 1997 (start RC). (e) Linear regressions for HMC and OSF corresponding to the r^2 in the red framed boxes. HMC = Hourly Magnetospheric Currents index; OSF = open solar flux.

given that the link between OSF and geomagnetic activity (section 2.2.2, relation 2) deteriorates as the averaging timescale falls below 1 year. Second, OSF is related to HMC more closely than to the other proxies (e.g., 0.62 for HMC and 0.54 for RC since 1997), which supports the usefulness of HMC for describing low-frequency changes in magnetospheric magnetic fields. Lastly, r^2 increases as the time series decrease in length, that is, as earlier times are excluded (Figure 7c). If the long-term trends (Table 1) are removed from the annual means of HMC and the reconstructed OSF prior to the calculation of r^2 , this effect weakens (0.68 instead of 0.61 since 1900) but still remains present. Apparently, there are mechanisms at work limiting r^2 by causing not only the trends but also a different kind of disagreeing variability among HMC and OSF.

Before we discuss two such mechanisms, it is important to recall that HMC and the reconstructed OSF are based on the same type of data, as OSF is reconstructed from the IDV(1d) and aa_c geomagnetic indices. Therefore, r^2 in Figure 7c is larger than it would be for annual means of the independently measured OSF ($r^2 = 0.8$ since 1974 and $r^2 = 0.88$ since 1997). Nevertheless, HMC and the reconstructed OSF do not share the same information, because the sets of observatories used to derive IDV(1d), aa_c , and HMC are disjunct, except for the years 1900–1910, when data from POT and SED are used for IDV(1d).

Table 1

Slopes of Piecewise Linear Fits to Annual Means of HMC and HMC_{No Bad} (or to Low-Pass Filtered Versions in Brackets), SN, F10.7 (Reconstructed), and OSF (Reconstructed)

Years	HMC (%)	HMC _{no bad} (%)	SN (%)	F10.7 (%)	OSF (%)
1900–1935	−59.9 (−60.1) ↓	−371.8 (−407.3) ↓	21.6	19.6	55.6 ↓
1935–1965	27.6 (28.2) ↑	27.6 (28.2) ↑	−21.9	7.1	1.6 ↓
1965–2012	25.5 (26.2) ↑	25.5 (26.2) ↑	−64.6	−26.0	−17.3 ↑
1900–2012	7.9 (8.4) ↑	−9.4 (−9.4) ↓	50.0	29.9	31.5 ↓

Note. Slopes are given in percent and refer to the level at the beginning of the time interval. Arrows indicate the direction of the slope in Figures 5c, 6, 7a, and 7b. HMC = Hourly Magnetospheric Currents index; SN = sunspot number; OSF = open solar flux.

The first mechanism is tied to the data from these geomagnetic observatories. The increasing degradation in geomagnetic data quality when moving to the past means that the magnetic signal from magnetospheric currents is increasingly “buried” under station specific measurement noise. This causes an artificial deviation between geomagnetic indices based on data from different stations. Thus, this mechanism can explain the limitation of r^2 between HMC and the measured/reconstructed OSF as well as the increase of r^2 with time.

The second mechanism is tied to the derivation method of HMC. Obviously, HMC and OSF are not as directly connected as suggested in section 2.2.2, likely because the second connection in relation 2 is compromised: The response of HMC to v_{sw} is probably not homogeneous, neither in space, nor in time. Finch et al. (2008) showed that geomagnetic data from high latitudes have a stronger dependence on v_{sw} than that from low latitudes. Since HMC includes data from stations at latitudes $14^\circ \leq \theta'_d \leq 75^\circ$, it is likely that the response to v_{sw} varies among them. Furthermore, the combination of observatories contributing to HMC varies irregularly with time (Figure 3). Thus, this mechanism can explain disagreements between OSF and HMC not caused by the first mechanism. In particular, it can help to explain the exceptional period 1935–1965, when (a) the trends in OSF and HMC are oppositely directed (Table 1), (b) r^2 between OSF and Dcx is greater than between OSF and HMC (Figure 7c), and (c) HMC is further offset from COV-OBS.x1 than at all other times (Figure 5d, gray).

The above points provide strong motivation for a future study focused on the individual responses of HMC observatories to the solar wind ($B \cdot v_{sw}^n$).

6. Conclusions

We have constructed the geomagnetic index HMC to investigate low-frequency variations in the magnetic signature of magnetospheric currents on ground since 1900. The greatest advantage of HMC over already existing indices is its reasonable absolute level and enhanced power at periods roughly between 1 and 11 years (solar cycle). In this frequency range, HMC is an improvement over the only other comparable long-term index, Dcx (since 1933). Annual means of HMC show a weak absolute linear decrease of 7.9% between 1900 and 2015, indicating that the strength of the magnetospheric currents, to which HMC is sensitive, may have decreased with time. The weakening of this long-term trend as compared to that in AMC (−35.4%) can be attributed to the data modifications performed, especially prior to ~1947. However, the long-term trend in HMC remains highly sensitive to the choice of early observatory data (prior to ~1935) and should be interpreted with caution.

We find that most of the low-frequency variability in HMC can be attributed to the reconstructed OSF (~60% since 1900 and ~96% since 1997) and that OSF is more closely related to HMC than to similar proxies (RC, Dcx, and q_{1M}^0 COV-OBS). The agreement between HMC and OSF is limited by the degrading geomagnetic data quality in the past and, probably, the inhomogeneous response of HMC observatories to solar wind forcing. Hence, these mechanisms could be responsible for the disagreement of trends in HMC and OSF (+31.46 % since 1900). However, most of this disagreement originates from an exceptional period roughly covering 1935 to 1965, when OSF agrees better with Dcx than with HMC, which in turn deviates noticeably from the COV-OBS.x1 external field measure. At this stage we cannot explain these peculiarities, which are subject of further investigation.

Acknowledgments

L. Pick thanks N. Olsen and C. Finlay for helpful discussions. The kinematically corrected OSF was kindly provided by M. Lockwood. We thank the anonymous referees for their suggestions that helped to improve the manuscript. L. Pick, M. Korte, and Y. Thomas acknowledge funding by the Deutsche Forschungsgemeinschaft (DFG) under project SPP1788 "Dynamic Earth"—DFG KO 2870/6-1. All publicly available third party material used is listed in Text S3. The HMC index, the modified observatory data, and a documentation of all modifications performed can be accessed via GFZ Data Services (Pick & Korte, 2018, <https://doi.org/10.5880/GFZ.2.3.2018.006>).

References

- Brown, W. J., Mound, J. E., & Livermore, P. W. (2013). Jerks abound: An analysis of geomagnetic observatory data from 1957 to 2008. *Physics of the Earth and Planetary Interiors*, 223, 62–76. <https://doi.org/10.1016/j.pepi.2013.06.001>
- Finch, I. D., & Lockwood, M. (2007). Solar wind-magnetosphere coupling functions on timescales of 1 day to 1 year. *Annales Geophysicae*, 25(2), 495–506. <https://doi.org/10.5194/angeo-25-495-2007>
- Finch, I. D., Lockwood, M. L., & Rouillard, A. P. (2008). Effects of solar wind magnetosphere coupling recorded at different geomagnetic latitudes: Separation of directly-driven and storage/release systems. *Geophysical Research Letters*, 35, L21105. <https://doi.org/10.1029/2008GL035399>
- Finlay, C. C., Lesur, V., Thébault, E., Vervelidou, F., Morschhauser, A., & Shore, R. (2017). Challenges handling magnetospheric and ionospheric signals in internal geomagnetic field modelling. *Space Science Reviews*, 206(1–4), 157–189. <https://doi.org/10.1007/s11214-016-0285-9>
- Finlay, C. C., Olsen, N., Kotsiaros, S., Gillet, N., & Tøffner-Clausen, L. (2016). Recent geomagnetic secular variation from Swarm and ground observatories as estimated in the CHAOS-6 geomagnetic field model. *Earth, Planets and Space*, 68(112), 18. <https://doi.org/10.1186/s40623-016-0486-1>
- Gannon, J. L. (2012). Assessing the validity of station location assumptions made in the calculation of the Geomagnetic Disturbance Index, Dst. *Space Weather*, 10, S02002. <https://doi.org/10.1029/2011SW000731>
- Ganushkina, N. Y., Liemohn, M. W., & Dubyagin, S. (2018). Current systems in the Earth's magnetosphere. *Reviews of Geophysics*, 56, 309–332. <https://doi.org/10.1002/2017RG000590>
- Gillet, N., Barrois, O., & Finlay, C. C. (2015). Stochastic forecasting of the geomagnetic field from the COV-OBS.x1 geomagnetic field model, and candidate models for IGRF-12. *Earth, Planets Space*, 67(71), 14. <https://doi.org/10.1186/s40623-015-0225-z>
- Gillet, N., Jault, D., Canet, E., & Fournier, A. (2010). Fast torsional waves and strong magnetic field within the Earth's core. *Nature*, 465, 74–77. <https://doi.org/10.1038/nature09010>
- Grayver, A. V., Munch, F. D., Kuvshinov, A. V., Khan, A., Sabaka, T. J., & Tøffner-Clausen, L. (2017). Joint inversion of satellite-detected tidal and magnetospheric signals constrains electrical conductivity and water content of the upper mantle and transition zone. *Geophysical Research Letters*, 44, 6074–6081. <https://doi.org/10.1002/2017GL073446>
- Harvey, K. L. (1992). The cyclic behavior of solar activity. In K. L. Harvey (Ed.), *The solar cycle* (Vol. 27, pp. 335), ASP conference series. San Francisco: ASP.
- Harvey, K. L. (1994). Irradiance models based on solar magnetic fields. *International Astronomical Union Colloquium*, 143, 217–225. <https://doi.org/10.1017/S0252921100024714>
- Karinen, A., & Mursula, K. (2006). Correcting the Dst index: Consequences for absolute level and correlations. *Journal of Geophysical Research*, 111, A08207. <https://doi.org/10.1029/2005JA011299>
- Kauristie, K., Morschhauser, A., Olsen, N., Finlay, C. C., McPherron, R. L., Gjerloev, J. W., & Opgenoorth, H. J. (2017). On the usage of geomagnetic indices for data selection in internal field modelling. *Space Science Reviews*, 206(1–4), 61–90. <https://doi.org/10.1007/s11214-016-0301-0>
- Krivova, N. A., & Solanki, S. K. (2004). Effect of spatial resolution on estimating the Sun's magnetic flux. *Astronomy and Astrophysics*, 417(3), 1125–1132. <https://doi.org/10.1051/0004-6361:20040022>
- Krivova, N. A., Vieira, L. E. A., & Solanki, S. K. (2010). Reconstruction of solar spectral irradiance since the Maunder minimum. *Journal of Geophysical Research*, 115, A12112. <https://doi.org/10.1029/2010JA015431>
- Lesur, V., Rother, M., Wardinski, I., Schachtschneider, R., Hamoudi, M., & Chambodut, A. (2015). Parent magnetic field models for the IGRF-12 GFZ-candidates. *Earth, Planets and Space*, 67(87), 15. <https://doi.org/10.1186/s40623-015-0239-6>
- Lockwood, M. (2013). Reconstruction and prediction of variations in the open solar magnetic flux and interplanetary conditions. *Living Reviews in Solar Physics*, 10(1), 4. <https://doi.org/10.12942/lrsp-2013-4>
- Lockwood, M., Barnard, L., Nevanlinna, H., Owens, M. J., Harrison, R. G., Rouillard, A. P., & Davis, C. J. (2013a). Reconstruction of geomagnetic activity and near-Earth interplanetary conditions over the past 167 yr—Part 1: A new geomagnetic data composite. *Annales Geophysicae*, 31(11), 1957–1977. <https://doi.org/10.5194/angeo-31-1957-2013>
- Lockwood, M., Barnard, L., Nevanlinna, H., Owens, M. J., Harrison, R. G., Rouillard, A. P., & Davis, C. J. (2013b). Reconstruction of geomagnetic activity and near-Earth interplanetary conditions over the past 167 yr—Part 2: A new reconstruction of the interplanetary magnetic field. *Annales Geophysicae*, 31(11), 1979–1992. <https://doi.org/10.5194/angeo-31-1979-2013>
- Lockwood, M., Nevanlinna, H., Barnard, L., Owens, M. J., Harrison, R. G., Rouillard, A. P., & Scott, C. J. (2014). Reconstruction of geomagnetic activity and near-Earth interplanetary conditions over the past 167 yr—Part 4: Near-Earth solar wind speed, IMF, and open solar flux. *Annales Geophysicae*, 32(4), 383–399. <https://doi.org/10.5194/angeo-32-383-2014>
- Lockwood, M., Owens, M., & Rouillard, A. P. (2009a). Excess open solar magnetic flux from satellite data: 1. Analysis of the third perihelion Ulysses pass. *Journal of Geophysical Research*, 114, A11103. <https://doi.org/10.1029/2009JA014449>
- Lockwood, M., Owens, M., & Rouillard, A. P. (2009b). Excess open solar magnetic flux from satellite data: 2. A survey of kinematic effects. *Journal of Geophysical Research*, 114, A11104. <https://doi.org/10.1029/2009JA014450>
- Lühr, H., & Maus, S. (2010). Solar cycle dependence of quiet-time magnetospheric currents and a model of their near-Earth magnetic fields. *Earth, Planets and Space*, 62(14), 843–848. <https://doi.org/10.5047/eps.2010.07.012>
- Milan, S. E., Clausen, L. B. N., Coxon, J. C., Carter, J. A., Walach, M.-T., Laundal, K., et al. (2017). Overview of solar wind-magnetosphere-ionosphere-atmosphere coupling and the generation of magnetospheric currents. *Space Science Reviews*, 206, 547–573. <https://doi.org/10.1007/s11214-017-0333-0>
- Mursula, K., & Karinen, A. (2005). Explaining and correcting the excessive semiannual variation in the Dst index. *Geophysical Research Letters*, 32, L14107. <https://doi.org/10.1029/2005GL023132>
- Olsen, N. (1993). The solar cycle variability of lunar and solar daily geomagnetic variations. *Annales Geophysicae*, 11(4), 254–262.
- Olsen, N., Lühr, H., Finlay, C. C., Sabaka, T. J., Michaelis, I., Rauberg, J., & Tøffner-Clausen, L. (2014). The CHAOS-4 geomagnetic field model. *Geophysical Journal International*, 197(2), 815–827. <https://doi.org/10.1093/gji/ggu033>
- Olsen, N., Sabaka, T. J., & Lowes, F. (2005). New parameterization of external and induced fields in geomagnetic field modeling, and a candidate model for IGRF 2005. *Earth, Planets and Space*, 57(BF03351897), 1141–1149. <https://doi.org/10.1186/BF03351897>
- Parker, E. N. (1958). Dynamics of the interplanetary gas and magnetic fields. *Astrophysical Journal*, 128, 664. <https://doi.org/10.1086/146579>
- Parker, E. N. (1963). *Interplanetary dynamical processes*. New York: Interscience Publishers.
- Pick, L. J. L., & Korte, M. (2017). An annual proxy for the geomagnetic signal of magnetospheric currents on Earth based on observatory data from 1900–2010. *Geophysical Journal International*, 211(2), 1223–1236. <https://doi.org/10.1093/gji/ggx367>
- Pick, L. J. L., & Korte, M. (2018). HMC index. GFZ Data Services. <https://doi.org/10.5880/GFZ.2.3.2018.006>

- Russell, C. T. (1971). Geophysical coordinate transformations. *Cosmic Electrodynamics*, 2, 184–196.
- Sabaka, T. J., Olsen, N., & Purucker, M. E. (2004). Extending comprehensive models of the Earth's magnetic field with Ørsted and CHAMP data. *Geophysical Journal International*, 159(2), 521–547. <https://doi.org/10.1111/j.1365-246X.2004.02421.x>
- Solanki, S. K., Schüssler, M., & Fligge, M. (2000). Evolution of the Sun's large-scale magnetic field since the Maunder minimum. *Nature*, 408, 445–447. <https://doi.org/10.1038/35044027>
- Solanki, S. K., Schüssler, M., & Fligge, M. (2002). Secular variation of the Sun's magnetic flux. *Astronomy and Astrophysics*, 383(2), 706–712. <https://doi.org/10.1051/0004-6361:20011790>
- Stamper, R., Lockwood, M., Wild, M. N., & Clark, T. D. G. (1999). Solar causes of the long-term increase in geomagnetic activity. *Journal of Geophysical Research*, 104(A12), 28,325–28,342. <https://doi.org/10.1029/1999JA900311>
- Sugiura, M. (1964). Hourly values of equatorial Dst for the IGY. *Annales of the International Geophysical Year*, 35, 4–45.
- Tapping, K. F. (2013). The 10.7 cm solar radio flux (F10.7). *Space Weather*, 11, 394–406. <https://doi.org/10.1002/swe.20064>
- Temerin, M., & Li, X. (2015). The Dst index underestimates the solar cycle variation of geomagnetic activity. *Journal of Geophysical Research: Space Physics*, 120, 5603–5607. <https://doi.org/10.1002/2015JA021467>
- Thébault, E., Finlay, C. C., Beggan, C. D., Alken, P., Aubert, J., Barrois, O., et al. (2015). International geomagnetic reference field: The 12th generation. *Earth, Planets and Space*, 67(79), 19. <https://doi.org/10.1186/s40623-015-0228-9>
- Thomson, A. W. P., & Lesur, V. (2007). An improved geomagnetic data selection algorithm for global geomagnetic field modelling. *Geophysical Journal International*, 169(3), 951–963. <https://doi.org/10.1111/j.1365-246X.2007.03354.x>
- Wardinski, I., & Holme, R. (2011). Signal from noise in geomagnetic field modelling: Denoising data for secular variation studies. *Geophysical Journal International*, 185(2), 653–662. <https://doi.org/10.1111/j.1365-246X.2011.04988.x>
- Wu, C.-J., Krivova, N. A., Solanki, S. K., & Usoskin, I. G. (2018). Solar total and spectral irradiance reconstruction over the last 9000 years. *Astronomy and Astrophysics*, 620(A120), 12. <https://doi.org/10.1051/0004-6361/201832956>
- Yamazaki, Y., & Maute, A. (2017). Sq and EEJ—A review on the daily variation of the geomagnetic field caused by ionospheric dynamo currents. *Space Science Reviews*, 206(1–4), 299–405. <https://doi.org/10.1007/s11214-016-0282-z>